Advances in Geo-Energy Research

Vol. 21, No. 3, p. 269-282, 2026

Original article

Residual fluid saturation in clayey silt hydrate-bearing sediments: Effects of porosity, hydrate saturation and pore habits

Yaobin Li[1,2], Tianfu Xu[1,2], Mengwei Liu[3], Yilong Yuan[1,2], Xin Xin[1,2]*

[1]*Key Laboratory of Groundwater Resources and Environment, Ministry of Education, Jilin University, Changchun 130021, P. R. China*

[2]*Jilin Provincial Key Laboratory of Water Resources and Environment, Jilin University, Changchun 130021, P. R. China*

[3]*Department of Ocean Science and Engineering, Southern University of Science and Technology, Shenzhen 518055, P. R. China*

Keywords:
Natural gas hydrates
hydrate habit
pore structure
residual saturation
clayey silt sediments

Cited as:
Li, Y., Xu, T., Liu, M., Yuan, Y., Xin, X. Residual fluid saturation in clayey silt hydrate-bearing sediments: Effects of porosity, hydrate saturation and pore habits. Advances in Geo-Energy Research, 2026, 21(3): 269-282.
https://doi.org/10.46690/ager.2026.09.06

Abstract:
Natural gas hydrate production is severely limited by residual methane and water from hydrate dissociation, primarily due to the inadequate understanding of hydrate morphology controls on dynamic residual fluid saturation. Traditional multiphase flow models adopt constant residual saturation and thus fail to capture *in-situ* reservoir dynamic responses. This limitation is pronounced in clayey silt hydrate reservoirs where fine-grained sediments produce high capillary pressure, and variable hydrate morphologies reshape pore structures, exacerbate fluid retention, as well as impair methane recovery efficiency and production safety. This study addresses this research gap via a self-developed low-temperature high-pressure multiphase displacement system. Therein, clayey silt cores with diverse initial porosities were prepared based on sediment properties of the Shenhu test area in the South China Sea. Excess-gas and excess-water approaches were used to replicate hydrate formation in gas-rich and water-rich environments, and residual fluid saturations were quantified under varied hydrate saturation. From the results, distinct residual saturation evolution patterns were identified: Residual water saturation exhibited two-stage power law growth with rising hydrate saturation, whereas residual gas saturation increased linearly. Higher initial porosity lowered residual fluid saturation, with porosity-induced differences amplified under high hydrate saturation. Water-rich environments yielded higher residual saturation than gas-rich counterparts, resulting from varied pore modifications caused by different hydrate morphologies. This study clarifies the morphology-governed dynamic evolution mechanisms of residual saturation in clayey silt hydrate sediments. The proposed dynamic saturation laws not only rectify deficiencies in traditional constant-saturation models but also provide robust parametric support for reservoir numerical simulation and offer fundamental guidance for safe, efficient and sustainable hydrate exploitation.

1. Introduction

Natural gas hydrates (NGH) are recognized as a highly strategically important future alternative energy source, characterized by vast reserves and high combustion efficiency. Widely distributed in deep-sea sediments and terrestrial permafrost regions, the industrial production of NGH furnishes a crucial material basis for optimizing the global energy structure and ensuring energy security (Agnissan et al., 2023).

NGH occur as solids in the pores of unconsolidated submarine sediments (Jiang et al., 2024). Exploitation necessitates the disruption of phase equilibrium, which induces the dissoci-

Yandy Scientific Press

*Corresponding author.
E-mail address: liyaobin@jlu.edu.cn (Y. Li); tianfu_xu@jlu.edu.cn (T. Xu); liumw@sustech.edu.cn (M. Liu); yilong@jlu.edu.cn (Y. Yuan); xxxx@jlu.edu.cn (X. Xin).
2207-9963 © The Author(s) 2026.
Received July 21, 2026; revised August 22, 2026; accepted September 1, 2026; available online September 3, 2026.

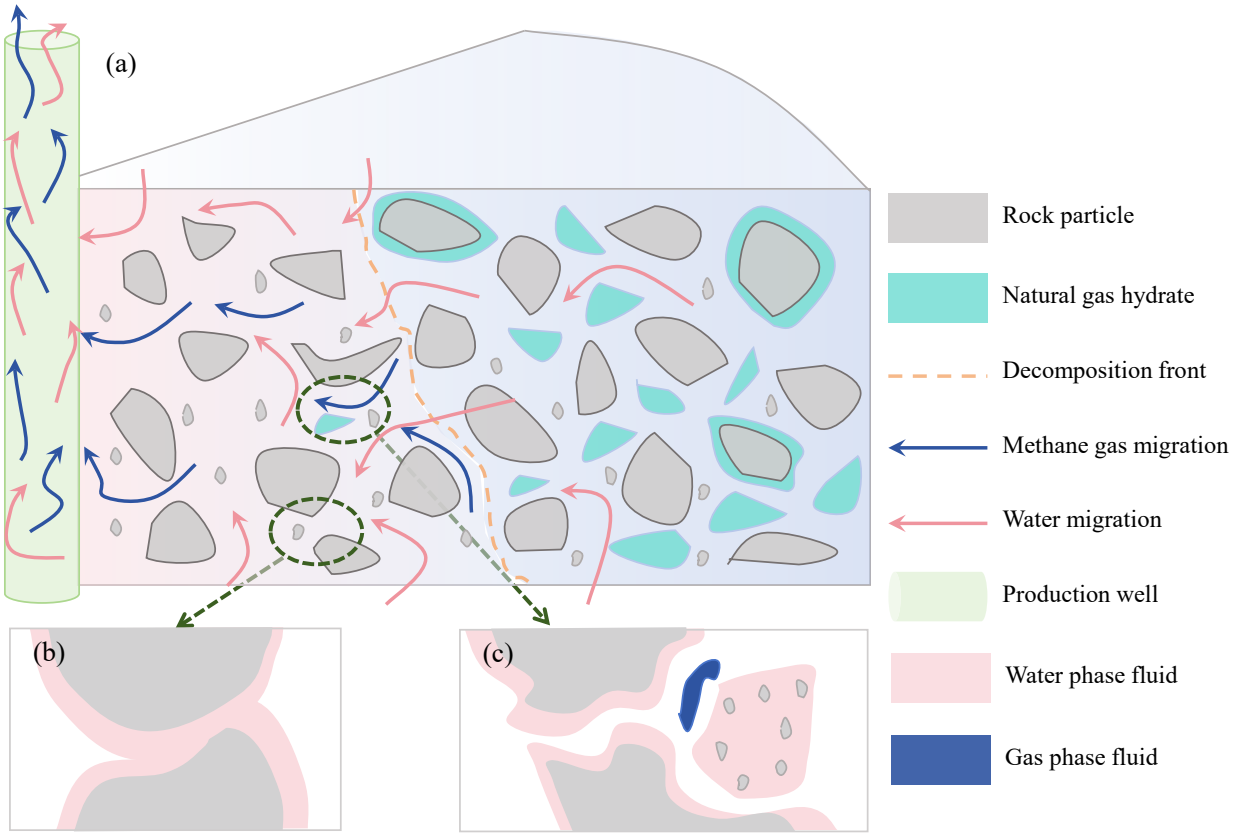


Fig. 1. Multiphase flow schematic for hydrate bearing sediments: (a) Reservoir scale hydrate dissociation and fluid migration, (b) pore-scale water blocking from capillary water bridging and (c) pore scale gas trapping by snap-off and ganglion isolation.

ation of solid hydrates into gaseous methane and liquid water, and subsequent recovery of methane via wellbores (Cai et al., 2020b; Meng et al., 2026). This process involves the coupled effects of hydrate phase transition and multiphase seepage (Gong et al., 2025; Zhang et al., 2026a) (Fig. 1(a)). Hydrate dissociation alters the sediment pore structure, which reverses the prior pore filling and particle cementation effects of intact hydrates, thereby enhancing porosity and pore connectivity (Cai et al., 2020a; Li et al., 2025a). With the reduced solid phase proportion, pore throats are dredged and the effective flow area is expanded, reducing flow resistance and capillary pressure, thereby promoting gas-liquid two phase flow (Cai et al., 2025; Cao et al., 2025).

Approximately 90% of global hydrates occur in marine clayey silt sediments, as estimated from global hydrate inventory syntheses (Li et al., 2024c; Tiong et al., 2025). These sediments contain fine particles, abundant clay minerals, narrow flow channels, and are characterized by low permeability and high capillary pressure, which dominate fluid migration (Wang et al., 2025b; Sun et al., 2026). Hydrates within these sediments develop distinct pore habits controlled by the formation conditions. Water-rich environments are dominated by pore-filling and load-bearing morphologies, occupying pore interiors and directly constricting flow pathways; whereas under gas-rich conditions, grain-coating and cementing morphologies prevail, adhering to grain surfaces and cementing particle contacts (Cai and Berg, 2025). Water predominantly flows along the edges of pore channels and is trapped in micropores under strong capillary pressure, forming the "water blocking effect" via capillary-induced water bridging (Fang et al., 2025) (Fig. 1(b)). In contrast, methane flows through pore-channel centers and encounters elevated flow resistance. It accumulates in micropores to form gas trapping (Fig. 1(c)), blocking originally unobstructed pore throats (Sun et al., 2025b). Core-scale displacement experiments and pore-scale numerical simulations have indicated that gas trapping and water blocking jointly reduce fluid migration efficiency by 50%-70% (Sun et al., 2025a). This reduction induces fluid retention, elevated methane partial pressure and heat accumulation (Chen et al., 2026). Consequently, local temperature and pressure revert to the hydrate stability zone. This state suppresses hydrate dissociation (Wang et al., 2025a; Zhang et al., 2026b) and triggers secondary hydrate formation (Guo et al., 2025; Kou et al., 2026). Residual saturation is a core parameter characterizing fluid retention effects in multiphase flow, defined as the proportion of immobile gas or water in pores relative to the total pore volume. Specifically, high residual water saturation (S_{rw}) intensifies water blocking, constricts gas flow channels, and exacerbates blockage risks from gas trapping. S_{rw} defines the capillary-trapped immobile water fraction in pore volumes, which resists displacement via gas flow or pressure drawdown (You et al., 2025). Residual gas saturation (S_{rg}), defined as the pore volume fraction of immobile gas trapped as disconnected ganglia and in dead-

end pores by capillary forces during water flow, sets the upper limit of methane recovery efficiency (Li et al., 2024b). Quantitative studies on residual saturation are therefore required to avoid deviations in NGH production plans induced by the misestimation of fluid retention effects.

Multiphase fluid flow in hydrate bearing sediments is an important global research focus, with extensive experimental studies yielding substantial advances. In this context, hydrate habit has been well characterized (Waite et al., 2009; Xia et al., 2025). In water-rich environments, hydrates predominantly grow within pores. At low hydrate saturation (S_h = 0.00-0.30), pore-filling hydrates prevail. These structures strengthen capillary trapping and elevate residual water saturation, while flow pathways persist in unoccupied pores. Meanwhile, at high hydrate saturation (S_h = 0.30-0.60), load-bearing hydrates dominate, which occlude pore channels, degrade transport properties, and alter residual fluid distribution by hindering fluid migration (Gao et al., 2024; Rake and Pinkert, 2024; Takahisa et al., 2025). In gas-rich environments, grain-coating hydrates dominate at low hydrate saturation (S_h = 0.00-0.20). Such hydrates minimally disturb pore channels, induce slight permeability reduction, and scarcely modify residual saturation owing to the limited pore reconstruction. At moderate hydrate saturation (S_h = 0.20-0.50), cementing hydrates prevail. They form cement layers at particle contacts, restrict interparticle fluid flow to lower residual fluid saturation, and further block pore channels (Zhang et al., 2024b; Wang et al., 2025c). Existing multiphase flow studies for hydrate bearing sediments primarily address flow-property evolution controlled by hydrate saturation. Cardona et al. (2023), Geranutti et al. (2024) and Li et al. (2024a) fabricated core samples of variable porosity and hydrate saturation and examined absolute permeability under triaxial compression, verifying that hydrate habit governs transport-property reduction. Song et al. (2024), Wang et al. (2024a) and Zhao et al. (2024) reported that hydrate occupancy shrinks effective pore volume and raises capillary pressure, and proposed van Genuchten model parameters for different hydrate saturations. Aghajanloo et al. (2024), Wu et al. (2024) and Li et al. (2025b) analyzed gas-water phase distributions and confirmed that variations in the geometry and size of dominant flow pores drive heterogeneous transport evolution. To reduce the computational complexity, current multiphase flow models commonly assign constant residual saturation (Cheng et al., 2025; Li et al., 2025c). This simplification prevents the real-time capture of dynamic residual gas and water evolution during hydrate dissociation and weakens reservoir dynamic feedback, thereby producing substantial discrepancies against field hydrate production (Zhang et al., 2024a; Xin et al., 2026). These constraints emphasize the requirement for the precise characterization of residual saturation evolution with hydrate saturation, with the ultimate goal of improving simulation fidelity.

This study aims to fill the research gap of dynamic hydrate-habit effects on residual fluid saturation and examine the multiphase flow characteristics of clayey silt hydrate-bearing sediments. To achieve this goal, a low-temperature high-pressure experimental system was developed that integrates three core modules: Constant-volume hydrate synthesis, multiphase flow displacement, and high-precision temperature-pressure control. Guided by the sediment properties of the Shenhu hydrate test area, representative clayey silt cores with diverse porosities were fabricated. Hydrates of varying saturations were synthesized via the excess-gas and excess-water methods, two prevalent approaches for laboratory hydrate preparation. The S_{rg} and S_{rw} corresponding to different pore structures were calculated by measuring displaced fluid volume. A quantitative correlation model between S_h and residual saturation (S_{rg} / S_{rw}) was established, and the influencing mechanism by which hydrate habit governs residual saturation was clarified. The findings provide key theoretical foundations for the safe and efficient production of hydrates in clayey silt reservoirs.

2. Experimental system

2.1 Experimental purpose and setup

The experiment aimed to reveal the regulatory mechanism of hydrate habit on residual gas and water saturation in gas-rich and water-rich environments, and to establish quantitative relationships between hydrate saturation and fluid residual saturation. The developed multiphase flow displacement experimental system for hydrate bearing sediments is compatible with a temperature range of -20-25 °C and a pressure range of 0-25 MPa (Fig. 2(f)). This system can accomplish core tasks including constant-volume synthesis of methane hydrates and multiphase flow displacement. The system comprises four key functional modules as described below.

2.1.1 Fluid supply module

The flow rate of liquid phase water is controlled by a peristaltic pump that is equipped with a high precision flow meter for the real-time monitoring of injection volume, thereby ensuring stable and metered supply of the aqueous phase. Methane gas is supplied by a high-pressure methane cylinder, with the gas pressure regulated via a high-pressure relief valve and quantitatively controlled by a high-pressure booster pump. The injection volume is recorded by a gas mass flow meter.

2.1.2 Core holding and temperature-pressure regulation module

The module is centered on a stainless steel cylindrical core holder (Hassler-type, inner diameter 50 mm), which was designed to accommodate an artificially configured clayey silt core. It is characterized by a temperature control range of -20-25 °C and a pressure-bearing capacity of 0-25 MPa, with a temperature fluctuation of $\leq$ 0.1 °C and pressure stability of $\leq$ 0.05 MPa. The *in-situ* reservoir thermobaric conditions can be accurately reproduced.

2.1.3 Stress sealing module

Composed of a confining pressure pump, an axial pressure pump, and an axial hydraulic cylinder, the module enables simulation of the *in-situ* stress state of hydrate reservoirs. With a fully sealed structural design, fluid leakage and gas escape are effectively prevented, and the stability of the pore structure and stress environment in the core is ensured.

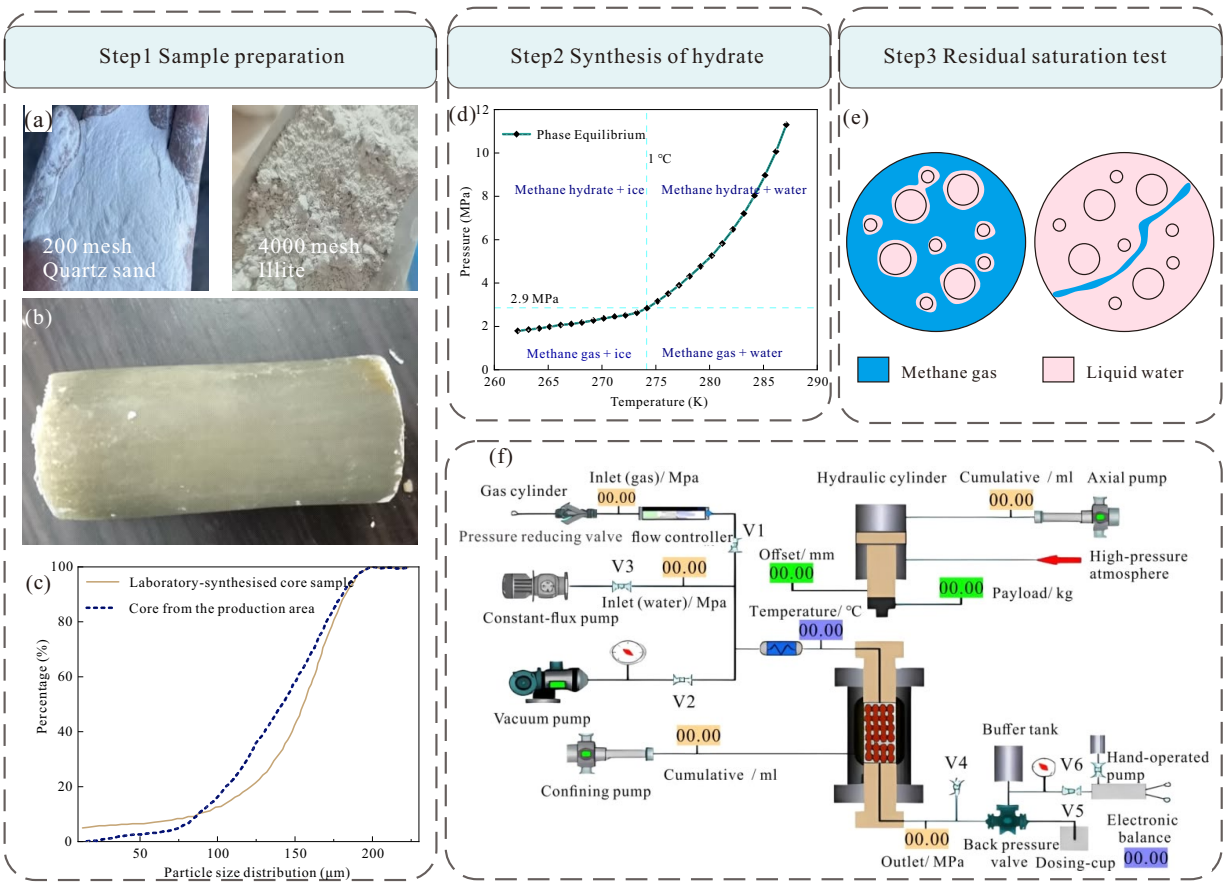


Fig. 2. Experimental apparatus and workflow for residual saturation characterization: (a) Experimental system, (b) raw quartz sand and illite materials, (c) compacted cylindrical core sample, (d) particle size verification, (e) phase equilibrium and experimental parameters and (f) pore scale fluid distribution pattern.

2.1.4 Data measurement and acquisition module

The system consists of temperature-pressure sensors for real-time *in-situ* thermobaric monitoring, a gas-liquid separator, phase-specific flowmeters, and a high-precision electronic balance. Reliable data support is provided for establishing quantitative relationships.

Under constant temperature and pressure, the designed experimental system supports continuous stable experiments. The coordinated control of functional modules preserves hydrate phase equilibrium and intact pore structures. This setup not only effectively characterizes hydrate spatial distributions in two typical environments but also quantifies multiphase seepage variations and residual saturation evolution controlled by distinct hydrate morphologies.

2.2 Experimental principle and procedure

Sediment *in-situ* porosity (φ) in the Shenhu area, South China Sea, was measured at 0.33-0.41, and hydrate saturation (S_h) was 0.15-0.47. Combining the field conditions, result universality and laboratory constraints, five core groups were designed with initial porosities of 0.10, 0.20, 0.30, 0.40 and 0.50. This porosity range fully encompasses the primary *in-situ* porosity interval of the Shenhu area and extends toward upper and lower boundary conditions arising from pronounced reservoir heterogeneity. The low-porosity end ($\varphi = 0.10$-0.20) corresponds to deeply buried, highly compacted clayey-silt intervals subject to intensive hydrate cementation, whereas the high-porosity end ($\varphi = 0.50$) represents shallow unconsolidated sedimentary layers. This extended gradient elucidates the complete regulatory effect of initial porosity on residual-saturation evolution and validates the general applicability of the proposed model over broad pore-structure conditions (Zhang et al., 2022; Liu and Santamarina, 2025).

Hydrate saturation was set at S_h = 0.00, 0.05, 0.10, 0.15, 0.20, 0.25, 0.30, 0.35, 0.40. This range encompasses the main *in-situ* saturation interval (0.15-0.40) of the Shenhu area and includes the low saturation interval (0.00-0.15) to establish a residual saturation baseline prior to hydrate formation. For safety and accuracy reasons, the upper limit was set at 0.40 rather than the field maximum of 0.47. Hydrate formation above 0.40 requires extremely high methane injection pressure (over 20 MPa in preliminary tests), which raises safety hazards and impairs saturation control accuracy. Furthermore, an upper limit of 0.40 can reflect the characteristics of high saturation hydrate reservoirs while ensuring experimental stability and repeatability. S_{rw} and S_{rg} were measured under varying hydrate saturations in gas-rich and water-rich environments.

Table 1. Mineral composition and content of sediments in the Shenhu Sea (%).

Component	Content	Component	Content
Quartz	27.27	Illite	7.24
Muscovite	18.68	Mont	6.84
Plagioclase	7.99	Chlorite	2.99
Orthoclase	3.6	Kaolinite	1.78
Calcite	19.83		

The experiment for each test group was repeated three times to reduce random errors and ensure experimental accuracy. The experimental principles and procedures are presented below.

2.2.1 Preparation of clayey silt core samples

Clayey silt cores were prepared following the particle size distribution and mineral composition of sediments from the Shenhu production test site, South China Sea (Table 1). The samples contained two components: A sand skeleton (200-mesh quartz sand, 75 μm) and clay minerals (4,000-mesh illite, 3.75 μm), mixed at a 4:1 mass ratio (Fig. 2(a)).

An appropriate amount of distilled water was added and uniformly stirred, with the moisture content regulated at 10%. Excess water was expelled during compaction. The mixed mineral particles were packed into a cylindrical pressure-resistant mold matched with an electric demolding device, followed by compaction and shaping using a hydraulic press (Fig. 2(b)).

The prepared clayey silt cores exhibited a radius (r) of 2.5 cm, a height (L) of 10 cm, and a total volume of 196.35 cm^3. The particle density of quartz sand (ρ_q) was 2.65 g/cm^3, and that of illite (ρ_i) was 2.60 g/cm^3. The masses of quartz sand (m_q) and illite (m_i) required for the preparation of cores with different porosity (φ) were calculated as follows (Table 2):

$$m_q = 0.8(1-\varphi)\pi r^2 L\rho_q \quad (1)$$

$$m_i = 0.2(1-\varphi)\pi r^2 L\rho_i \quad (2)$$

To determine the particle size composition of the prepared clayey silt cores, a BT-9300LD laser particle size analyzer was employed. The measured particle size composition was compared with that of actual sediments from the hydrate production test area (Liu et al., 2025). The two exhibit similar particle size distributions (Fig. 2(c)), so artificial cores can be utilized as substitutes for actual hydrate bearing sediment cores in flow property tests. It should be noted that not all microstructural features of natural sediments (e.g., primary sediment fabric, natural clay aggregation, *in-situ* cementation) can be fully reproduced by artificial cores. Natural sediments of the Shenhu area contain multiple clay minerals, including montmorillonite, illite, chlorite, and kaolinite. Illite was selected as the clay component; as the dominant clay mineral in the study area, illite is capable of representing fundamental pore-scale capillary and seepage properties of clayey-silt sediments (Lei et al., 2024). Artificial cores permit the precise control of experimental variables and mitigate background heterogeneity, enabling independent evaluations of porosity, hydrate saturation and hydrate morphology effects on residual saturation. The derived evolutionary relationships and model framework are universally applicable to clayey silt hydrate bearing sediments. Nevertheless, site-specific calibration based on natural core samples is required for the accurate quantitative prediction of target reservoirs.

2.2.2 Constant-volume synthesis of methane hydrates

In the hydrate synthesis process, metered methane and deionized water are injected into the cores. One volume of methane hydrate decomposes into 0.8 volumes of liquid water (Makogon et al., 2007; Wu et al., 2025). Accordingly, the injected deionized water volume (V_w) was set to 0.8 times the target hydrate volume (V_h) for stoichiometric balance and precise saturation control. System temperature was lowered to phase equilibrium conditions conducive to hydrate formation. The phase equilibrium curve of methane hydrates in pure water systems (Fig. 2(d)) indicates an equilibrium pressure of 2.9 MPa at 1 °C, which was adopted as the hydrate synthesis condition in this study. It should be noted that these stoichiometric formulas are derived for ideal pure methane-pure water hydrate systems. Systematic deviations are therefore introduced when the formulas are applied to clayey silt sediments rich in fine clay particles (Kim et al., 2022). Most injected water is tightly adsorbed as bound water on clay mineral surfaces and does not participate in hydrate crystallization, thereby decreasing the free water available for hydrate formation. To mitigate this effect and guarantee accurate saturation control, targeted strategies were implemented for the two synthesis methods. For the excess-gas method, excess methane drives all free pore water into hydrate formation, and the constant fraction of immobile bound water under standardized sample preparation does not impair the relative accuracy of the saturation gradient. For the excess-water method, injected methane is fully converted to hydrate under water-excess conditions, while clay-bound water constitutes a fixed fraction of total water and does not interfere with methane-to-hydrate conversion efficiency.

Hydrate volume (V_h), methane gas volume (V_g), and deionized water volume (V_w) were calculated separately to synthesize hydrates of varying saturation (S_h) (Yang et al., 2026) (Tables 3 and 4):

$$V_h = V_p S_h \quad (3)$$

$$V_w = 0.8V_h \quad (4)$$

$$V_g = \frac{V_h}{164} \quad (5)$$

The excess-gas method was employed for hydrate synthesis to characterize hydrate habit at different saturation in gas-rich environments. Following the principle of "excess gas and fixed water volume", deionized water was injected into the core via a peristaltic pump at a flow rate of 2 mL/min, with the injection volume set as V_w. The core was then left undisturbed for 2 h to ensure uniform liquid phase distribution. A high-pressure methane cylinder was activated, and methane gas was depressurized via a pressure relief valve, quantitatively controlled by a booster pump, and supplied at 30 mL/min.

Table 2. Contents and volumes of components in clayey silt core samples.

Porosity	Total mass (g)	Quartz sand (g)	Illite (g)	Water content (g)	Pore volume (cm^3)
0.10	463.70	371.81	91.89	46.37	19.64
0.20	412.18	330.50	81.68	41.22	39.27
0.30	360.66	289.18	71.47	36.07	58.91
0.40	309.13	247.87	61.26	30.91	78.54
0.50	257.61	206.56	51.05	25.76	98.18

Table 3. Gas-phase volume under varying saturation and porosity (cm^3).

Porosity	Hydrate saturation							
	0.05	0.10	0.15	0.20	0.25	0.30	0.35	0.40
0.10	161.1	322.1	483.1	644.2	805.2	966.3	1,127.3	1,288.4
0.20	322.8	645.7	968.5	1291.3	1,614.2	1,937.0	2,259.8	2,582.7
0.30	483.1	966.1	1,449.2	1,932.2	2,415.3	2,898.3	3381.4	3,864.5
0.40	644.0	1,288.1	1,932.1	2,576.1	3,220.1	3,864.2	4,508.2	5,152.2
0.50	805.1	1,610.1	2,415.2	3,220.3	4,025.4	4,830.5	5,635.5	6,440.6

A gas flow controller monitored the injection volume in real time, which was maintained to be higher than V_g. The system temperature was lowered to 1 °C. Hydrate formation induced a continuous pressure drop in the reaction column. Hydrate formation was deemed complete when the gas flow meter reading remained stable for two consecutive hours and pressure stabilized at 2.8-2.9 MPa (Joseph et al., 2017).

The gas-rich initial state is jointly verified by three complementary lines of evidence. First, water acts as the limiting reactant in the excess-gas method. The volume of injected water is stoichiometrically matched to the target hydrate content. Methane is supplied in excess, which ensures that all free pore water is theoretically fully converted into solid hydrate. Second, system-pressure stabilization at hydrate-phase-equilibrium conditions over two consecutive hours signals complete consumption of free water and termination of hydrate formation. Third, no continuous liquid-water outflow is detected during subsequent nitrogen pre-displacement, further confirming the absence of mobile free water within pore spaces (Golsanami et al., 2026). Core pores are dominated by hydrates and free methane gas (Wang et al., 2024b), confirming the gas-rich initial state for residual saturation measurement.

The excess-water method was adopted for hydrate synthesis to characterize hydrate habit at different saturation in water-rich environments. Deionized water was injected into the core via a peristaltic pump until saturation, with the injection volume set as V_p. Methane gas (V_g) was injected via a booster pump, and the system was allowed to stand for 1 hour to facilitate gas dissolution. The temperature was lowered to 1 °C. After pressure stabilization, methane was completely converted into hydrates. Core pores are mainly composed of hydrates and liquid water, confirming the water-rich initial state for residual saturation measurement.

To further verify and calibrate actual hydrate saturation, unreacted residual methane volume within the core was measured upon synthesis equilibrium. The actual hydrate volume was derived by subtracting residual-gas volume (converted to standard temperature and pressure) from the total injected methane volume using the molar-volume ratio of methane hydrate. Deviations between calibrated actual S_H and theoretical target S_h remained below 0.03 for all experimental groups. This error primarily stems from trace methane dissolved in pore water and the systematic error of the gas mass flow meter, falling within the acceptable range for conventional hydrate synthesis experiments.

2.2.3 Measurement of residual saturation

After hydrate synthesis, the core remains in phase equilibrium. Measuring residual gas saturation via water displacement in gas-rich conditions, or residual water saturation via methane displacement in water-rich conditions, may induce new hydrate nucleation and disrupt the core pore structure. To avoid secondary hydrate formation and pore structure disturbance from methane water contact during residual saturation tests, inert nitrogen was adopted to isolate the two phases.

Nitrogen constitutes a methodologically sound inert surrogate for methane. First, nitrogen and methane behave as non-wetting phases within water-wet clayey-silt sediments. Their residual trapping is governed by pore-geometry-dependent capillary mechanisms rather than gas identity, yielding consistent pore-scale distribution patterns. Second, under experimental conditions, methane-water and nitrogen-water systems exhibit minor differences in gas-water interfacial tension, exerting negligible effects on capillary entry pressure and residual-

Table 4. Liquid phase volume under varying saturation and porosity (cm^3).

Porosity	Hydrate saturation							
	0.05	0.10	0.15	0.20	0.25	0.30	0.35	0.40
0.10	0.8	1.6	2.4	3.1	3.9	4.7	5.5	6.3
0.20	1.6	3.2	4.7	6.3	7.9	9.5	11.0	12.6
0.30	2.4	4.7	7.1	9.4	11.8	14.1	16.5	18.9
0.40	3.1	6.3	9.4	12.6	15.7	18.9	22.0	25.1
0.50	3.9	7.9	11.8	15.7	19.6	23.6	27.5	31.4

trapping efficiency. Third, both gases show extremely low pore-water solubility under test conditions, and the solubility differences produce no measurable bias in trapped-residual-gas volume calculations. Finally, neither gas undergoes specific adsorption or chemical interactions with quartz and clay-mineral surfaces, so the sediment wettability and pore structure remain unaltered. This inert-substitution approach has been well-validated and widely adopted in prior seepage experiments on hydrate-bearing sediments (Seol and Kneafsey, 2011; Li et al., 2022a).

The residual saturation test comprised three procedural steps, with specific objectives and detailed operations as follows:

i) Nitrogen pre-displacement: Isolate methane and water phases and suppress secondary hydrate formation.

Inject nitrogen into the core at a constant flow rate of 30 mL/min, with injection pressure set 0.5 MPa above the hydrate phase equilibrium pressure to guarantee sufficient driving force. Injection proceeds until no residual methane or liquid water discharges from the core outlet, fully saturating pore spaces with pure nitrogen. This step completes phase isolation and prevents secondary hydrate formation in subsequent displacement.

ii) Residual gas saturation measurement for gas-saturated cores: Simulate water-driven gas migration via water displacing nitrogen to determine residual gas saturation.

Using nitrogen as an inert methane substitute to mimic reservoir gas phase and avoid hydrate reformation, inject deionized water at 2 mL/min to displace nitrogen from the pre-saturated core. Record the displaced nitrogen volume (V_{dg}) at the outlet is recorded in real time. Displacement ceases when the gas flow rate remains stable for one hour and the core pressure difference plateaus. The S_{rg} is calculated via Eq. (6).

iii) Residual water saturation measurement for water-saturated cores: Simulate gas-driven water migration via nitrogen displacing water to determine residual water saturation.

For fully water-saturated cores, nitrogen was injected at 30 mL/min to displace pore water, with the displaced water volume (V_{dw}) recorded in real time. Displacement terminated after one hour of stable liquid flow and steady core pressure difference. The S_{rw} was calculated via Eq. (7):

$$S_{rg} = 1 - \frac{V_{dg}}{V_p} \tag{6}$$

$$S_{rw} = 1 - \frac{V_{dw}}{V_p} \tag{7}$$

3. Experimental results and analysis

The quantitative data of S_{rw} and S_{rg} were acquired through the aforementioned experimental procedures. The data encompassed combined conditions of different initial porosity, hydrate saturation, and gas-rich/water-rich environments (Fig. 3).

3.1 Effect of hydrate saturation

In both water-rich and gas-rich environments, the S_{rg} and S_{rw} of clayey silt cores with different initial porosities exhibit an increasing trend with increasing S_h. A typical core from the Shenhu area (φ = 0.30) was selected as a case study to illustrate the variation. Water-rich environment: At S_h = 0.0, $S_{rw} \approx 0.48$ and $S_{rg} \approx 0.11$. When S_h increases to 0.20, S_{rw} rises to 0.70 (a 46% increase) and S_{rg} reaches around 0.19 (an absolute increase of 0.08). As S_h further rises to 0.40, S_{rw} approximates 0.82 (a 25% increase) and S_{rg} reaches 0.28 (an absolute increase of 0.09). Gas-rich environment: At S_h = 0.0, $S_{rw} \approx 0.42$ and $S_{rg} \approx 0.06$. When S_h increases to 0.20, the S_{rw} increases to about 0.56 (a 33% increase) and S_{rg} rises to 0.11 (an absolute increase of 0.05). As S_h climbs to 0.40, the S_{rw} reaches approximately 0.65 (a 21% increase) and S_{rg} approximates 0.16 (an absolute increase of 0.05). All the above percentage values were calculated from the mean of three replicate tests, with a measurement standard deviation no greater than 3%. S_{rw} presents a two-stage evolution characteristic with increasing S_h: A sharp rise at low S_h and a gradual increase at high S_h. The transition point between these two stages stabilizes at $S_h \approx 0.20$. In contrast, S_{rg} maintains a steady increasing trend as S_h rises, without obvious stage characteristics. A comparative analysis of datasets from all five initial porosity groups revealed no systematic shift of this transition point with changing initial porosity. This stability originates from a critical state where pore-filling hydrates block dominant seepage throats. The state is controlled by relative pore-size distribution rather than absolute porosity. Cores with different porosities have consistent particle gradation and compaction characteristics, maintaining similar relative pore-size distributions and comparable transition saturation.

In clayey silt hydrate bearing sediments, the observed two-

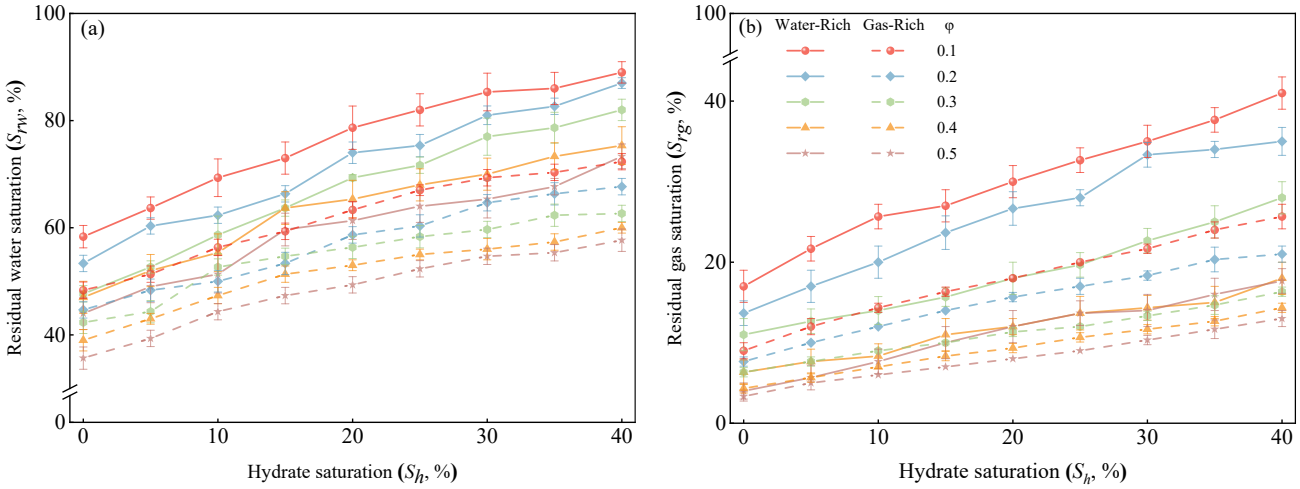


Fig. 3. Variations in residual fluid saturation with hydrate saturation under different initial porosities: (a) Residual water saturation shows a two-stage increase and (b) Residual gas saturation rises linearly.

stage increase in residual water saturation with rising hydrate saturation is consistent with a pore-throat-controlled drainage regime coupled with a preferential hydrate habitat. At low S_h, hydrate tends to nucleate and grow within the relatively larger pores and critical pore throats, where its presence most effectively elevates capillary entry pressures and obstructs key drainage pathways (Lei et al., 2019; Feng et al., 2023). These high-connectivity conduits exert a disproportionate control on fluid mobility within fine-grained pore networks (Jang et al., 2011; Liu and Seol, 2025). Even minor hydrate occupancy can substantially elevate residual water saturation. Smaller pores cannot be invaded by gas or pressure drawdown, and water remains trapped as corner films and micropore water. The inflection point stabilizes at approximately S_h = 0.20, likely representing a geometric and connectivity threshold at which macropore pathways critical for drainage are partially occluded. Beyond this stage, the remaining mobile-water fraction is increasingly constrained by micropore capillarity, such that additional hydrate growth primarily reduces pore volume in a more spatially uniform manner or occupies secondary pore space. Consequently, residual water saturation increases only gradually at higher S_h.

In contrast, residual gas saturation increases monotonically with hydrate saturation without a distinct two-stage evolution. This behavior is consistent with a water-wet system, in which gas serves as the non-wetting phase and trapping arises from snap-off and ganglion isolation during imbibition (Jang et al., 2016; Li et al., 2022a). Rising hydrate saturation progressively introduces additional pore constrictions, dead-end pores and local heterogeneities, increasing pore-throat geometries capable of disrupting gas continuity. Residual water is highly sensitive to the early loss of a few major drainage conduits. Meanwhile, residual gas saturation follows a different pattern: It is controlled by the cumulative density of snap-off sites and the gradual fragmentation of gas pathways across the pore network. The resulting response is a quasi-linear, continuously increasing residual gas saturation as S_h rises, even though the underlying pore scale trapping processes remain highly heterogeneous.

3.2 Effect of initial porosity

At a constant S_h, both S_{rg} and S_{rw} decrease monotonically with increasing initial porosity. As porosity increases from 0.10 to 0.50, a significant decrease in fluid residual saturation is observed. In water-rich environments, at S_h=0.20, the S_{rw} decreases from 0.78 to 0.61 and S_{rg} from 0.30 to 0.12. At S_h=0.40, the S_{rw} drops from 0.90 to 0.71 and S_{rg} from 0.41 to 0.17. The difference in residual saturation evolution among cores with varying initial porosity is more pronounced under high S_H conditions.

At a fixed S_h, increasing the initial porosity of clayey silt typically implies (i) a larger characteristic pore size and throat radius, (ii) better-connected flow pathways, and (iii) lower capillary entry pressures for invasion and drainage. In low-porosity cores, the pore-throat network approaches its capillary and connectivity limits. Pore-filling hydrates preferentially occupy or constrict drainage-critical throats, severely obstructing gas flow pathways and trapping substantial water within micropores and corner films (Li et al., 2022a). As porosity rises, the network contains more redundant pathways and wider throats; thus, even with identical S_h, hydrate-induced occlusion is less likely to collapse global connectivity. This reduces the degree of drainage suppression and explains the monotonic decline in residual water saturation with increasing porosity (Li et al., 2025b).

Once again, residual gas is controlled largely by snap-off and ganglion isolation during imbibition. Low-porosity networks likely exhibit stronger pore-body-to-throat contrast and more abundant, closely spaced throat-scale bottlenecks, increasing the probability of snap-off and gas disconnection during imbibition. Higher initial porosity leads to larger throats and better connectivity, reducing both the chance of snap-off and the probability that gas clusters become hydraulically isolated. Hydrate at a fixed S_h still add constrictions; yet in higher-porosity sediments, these added barriers do not multiply trapping sites as efficiently as they do in an already throat-

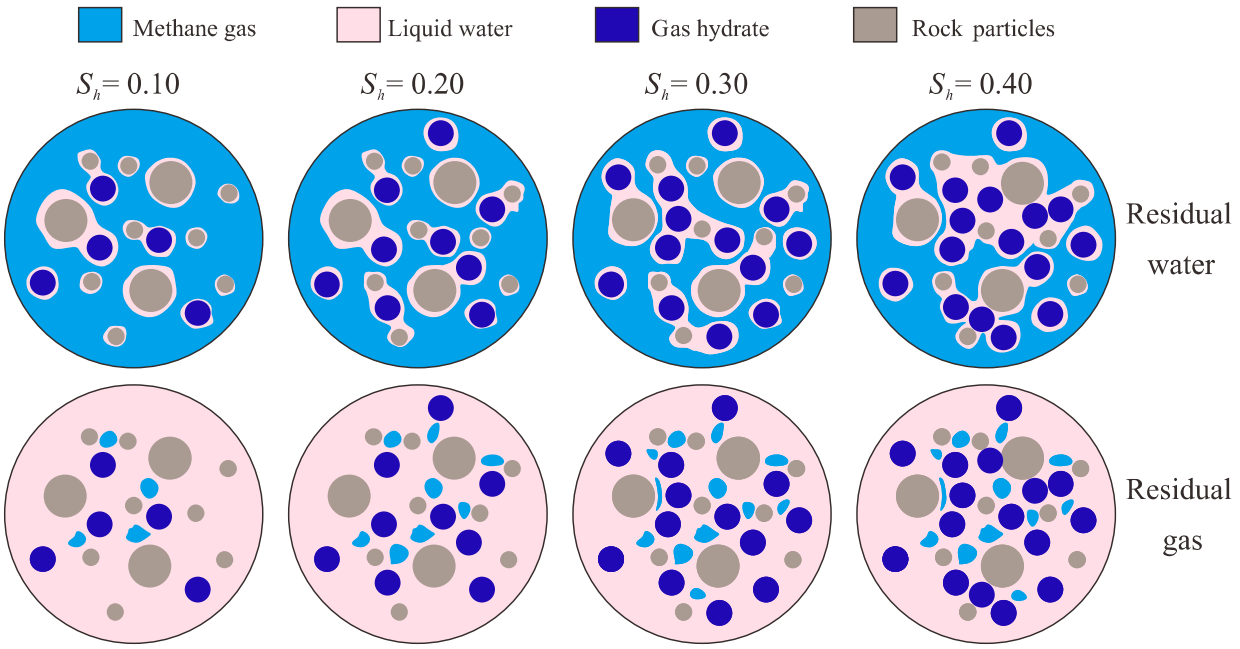


Fig. 4. Pore scale schematic of residual fluid distribution under water-rich conditions with varying hydrate saturation. The upper and lower panels show progressive residual water trapping and gas accumulation during increasing pore-filling hydrate saturation.

limited, low-porosity system.

At high S_h, a stronger modification effect on the pore structure is exerted by hydrate formation. Throats in low-porosity cores are easily completely blocked by load-bearing/cementing hydrates, whereas high-porosity cores retain partial connected channels. This further amplifies the fluid residual saturation difference among cores with varying initial porosity.

3.3 Effect of hydrate pore habit

Notably, the hydrate pore habit effects discussed in this section are inferred from the employed synthesis methods and established morphological findings from prior studies, rather than direct *in-situ* pore imaging in our experiments (Terzariol et al., 2020).

Under identical initial porosity and S_h, the residual saturation in a water-rich environment is consistently higher than that in a gas-rich environment. The difference in S_{rw} ranges from 0.06 to 0.22, while the difference in S_{rg} varies between 0.02 and 0.12. These residual saturation differences exhibit an "initial increase followed by stabilization" trend as S_h increases, which is highly synchronized with the phasic transition of hydrate habit. Quantitatively, stabilization begins at approximately $S_h = 0.30$. Within the interval of $S_h = 0.30$-0.40, the residual water saturation difference between the two environments stabilizes at 0.17-0.22, and the residual gas saturation difference remains at 0.09-0.12, with no notable further expansion as saturation increases. This phenomenon essentially stems from the differential modification of pore structure by distinct hydrate occurrence habit.

Hydrates predominantly grow within pore spaces in water-rich systems (Fig. 4) and nucleate on particle surfaces in gas-rich systems (Lv et al., 2020). Such formation habit differences account for the consistently higher residual saturations observed in water-rich environments under identical initial porosity and hydrate saturation. In the water-rich case, intra-pore hydrate growth directly reduces the effective flow volume and preferentially constricts drainage-dominant pore throats. At S_h < ~0.20, pore-filling hydrates distributed across micro- and mesopores diminish mobile water fractions and expand solid-water interfacial areas, enhancing adsorbed water retention and elevating residual water saturation. As S_h exceeds approximately 0.20, hydrates transition into load-bearing structures that form continuous cross-throat bridging networks. This geometry narrows critical drainage conduits and increases capillary entry pressure, hindering water displacement and yielding higher residual water saturation than gas-rich systems. The same structural change also increases residual gas saturation; it partitions the network and increases the density of throat-scale barriers that cause snap-off and ganglion isolation during imbibition, which traps methane as disconnected clusters. In contrast, gas-rich formation leads to grain-coating and cementing hydrate habits, which mainly modify pore boundaries and particle contacts, with less effect on pore volume and overall connectivity (Fig. 5). Thin grain coatings at low hydrate saturation occupy little pore volume directly. Cementation at higher hydrate saturation may locally narrow throats but does not cause widespread cross-throat bridging. Consequently, both drainage inhibition and imbibition trapping are less efficient, leading to lower both residual water and gas saturation relative to water-rich cases.

3.4 Fluid residual saturation model

Residual fluid saturation and its evolution vary with the sediment lithology, burial depth, grain size distribution, clay

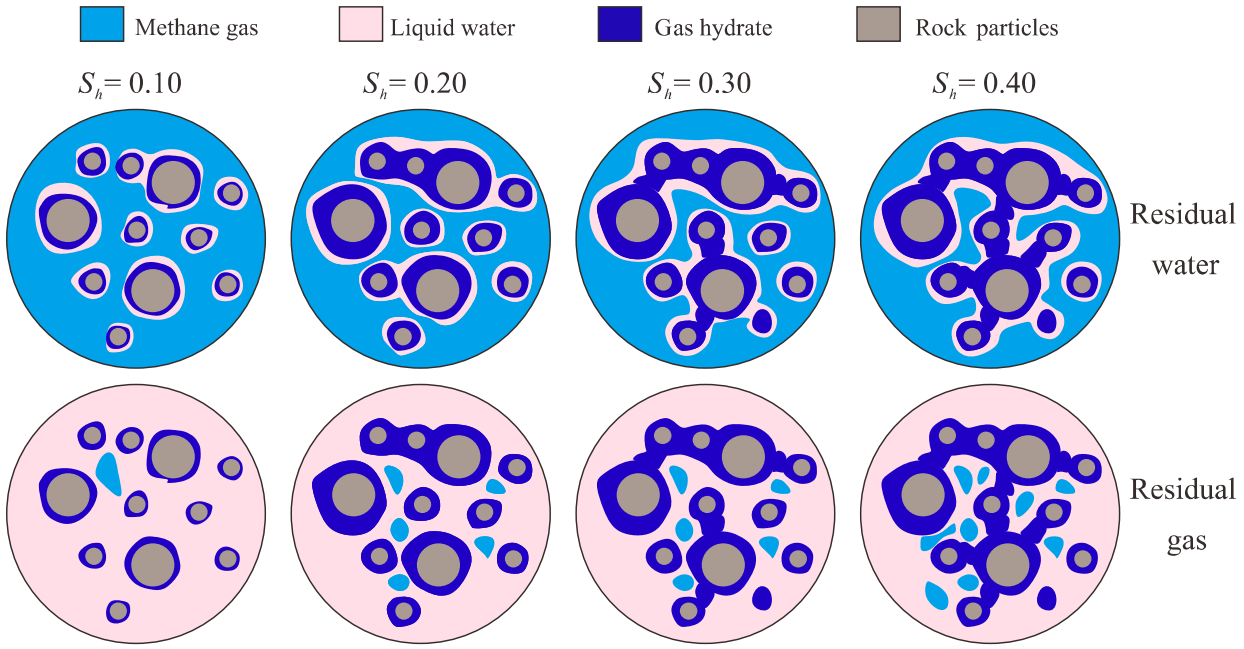


Fig. 5. Pore scale schematic of residual fluid distribution under gas-rich conditions with varying hydrate saturation. The upper and lower panels show progressive residual water trapping and gas accumulation during increasing grain-coating/cementing hydrate saturation.

content, initial porosity, and hydrate formation conditions. To reduce background parameter interference, the concept of normalized residual saturation (S_{nrw}, S_{nrg}) is introduced. This metric mitigates disparities in intrinsic sediment parameters and helps uncover the core physical mechanism: Hydrate-saturation and pore-habit driven pore-structure evolution governs multiphase seepage and residual-saturation behavior in hydrate-bearing sediments (Awag et al., 2024). Notably, this normalization cannot fully eliminate effects from initial porosity, pore-size distribution and pore connectivity. It extracts the universal evolutionary trend of residual saturation against hydrate growth, whereas absolute residual-saturation magnitudes preserve geological heterogeneity originating from initial pore structures. A higher relative residual saturation corresponds to a stronger evolutionary response to variations in S_h:

$$S_{nrw} = \frac{S_{rw}(h)}{S_{rw0}} \tag{8}$$

$$S_{nrg} = \frac{S_{rg}(h)}{S_{rg0}} \tag{9}$$

where S_{rw0}, and S_{rg0} represent residual water and gas saturation of the core, respectively, in the absence of hydrates; $S_{rw}(h)$, and $S_{rg}(h)$ are residual water and gas saturation of the core, respectively, at a specific hydrate saturation S_h.

Distinctions between absolute and normalized residual saturation bear specific implications for hydrate-pore-habit effects. Absolute residual saturation quantifies the actual fraction of immobile fluid within the pore space, jointly governed by initial pore-structure baselines and modification intensity from hydrate growth. Inter-sample disparities in absolute residual saturation arise from initial fluid-distribution backgrounds (water-rich systems possess higher residual-water baselines even in the absence of hydrates) and differential pore occlusion induced by distinct hydrate morphologies. By contrast, normalized residual saturation removes initial-baseline offsets and isolates evolutionary patterns driven solely by hydrate accumulation. The consistent evolutionary trends following normalization demonstrate that hydrate habits mainly modulate the magnitude and rate of residual-saturation growth, without altering the fundamental physical mechanisms governing fluid trapping.

3.4.1 Residual water saturation (S_{rw}) evolution model

The evolution of S_{rw} conforms to the power-law relationship (Fig. 6(a)):

$$S_{nrw} = 1 + \alpha S_h^{\beta} \tag{10}$$

where α denotes the liquid phase growth coefficient, which reflects the relative increase of S_{rw} during hydrate formation; β denotes the power exponent, which reflects the change trend of the growth rate: When β is less than 1, the growth rate decreases with the increase of S_h.

Least squares fitting yields values of α and β of 1.10 and 0.50 for water-rich environments, and 1.20 and 0.78 for gas-rich environments, respectively. Power-law fitting yields coefficients of determination (R^2) of 0.8303 and 0.9783, and root mean squared errors of 0.1978 and 0.0243 under water-rich and gas-rich conditions. This indicates that compared with gas-rich environments, the S_{rw} in water-rich environments exhibits a more significant overall increase and a more drastic attenuation of growth rate with S_H. This phenomenon is essentially attributed to the differential influence of hydrate habit on pore-fluid interactions. For the water-rich environment, at the low S_h stage, pore-filling hydrates preferentially occupy

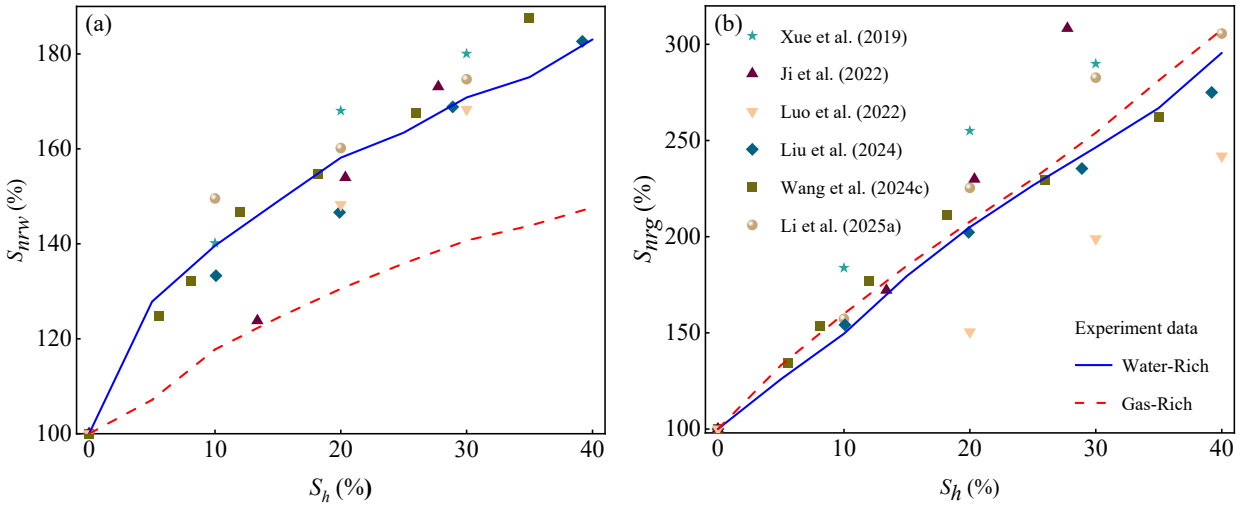


Fig. 6. Normalized saturation models and cross-study validation: (a) Power-law model for residual water saturation and (b) linear model for residual gas saturation.

micro-pores, which rapidly thickens the adsorbed water film on particle surfaces and enhances the capillary trapping effect, thereby inducing a substantial initial increase in S_{rw} (high α). At the high S_h stage, load-bearing hydrates form a continuous framework across pore throats, as the micro-pore space available for water retention approaches saturation, the growth rate of S_{rw} attenuates rapidly (low β). For the gas-rich environment, at the low S_h stage, grain-coating hydrates merely coat particle surfaces without occupying flow channels, resulting in a minor initial growth amplitude of S_{rw} (low α). At the high S_h stage, cementing hydrates accumulate at particle contact points, causing minimal pore structure modification and thus leading to a gentle attenuation of S_{rw} growth rate (high β).

Consistent with existing experimental studies, S_{rw} exhibits a two-stage evolutionary pattern, namely "a sharp rise at low S_h (0.00-0.20) and a gradual increase at high S_h (0.20-0.40)". This pattern can be accurately characterized by the established power-law model. S_{nrw} exhibits better fitting with experimental data from water-rich environments, a phenomenon attributed to the fact that hydrates in these studies were synthesized via the excess water method. This method leads to the transition of hydrate habit from pore-filling to load-bearing, while hydrate habit characteristics between water-rich and gas-rich environments are not accurately distinguished in most of previous investigations. The proposed S_{rw} evolution model quantitatively characterizes the differential regulatory mechanisms of distinct hydrate pore habits on residual water saturation. The method systematically covers the two typical "water-rich/gas-rich" environments and is featured with directly invokable parameters, which complements the limitation that existing studies are mostly established under a single formation condition.

3.4.2 Residual gas saturation (S_{rg}) evolution model

The S_{rG} evolution conforms to a linear relationship (Fig. 6(b)):

$$S_{nrg} = 1 + \varepsilon S_h \tag{11}$$

where ε represents the gas phase growth coefficient, which reflects the relative increase of S_{rg} during hydrate formation.

Under gas-rich and water-rich environments, a consistent evolutionary trend is exhibited by S_{rg}. An ε value of 5 is obtained via least squares fitting, which verifies that a limited influence of hydrate habit on residual gas distribution is exerted. Linear fitting produces R^2 of 0.8904 and 0.9364, and root mean squared errors of 0.1713 and 0.1446 for water-rich and gas-rich environments, respectively. A strong linear correlation is validated between normalized residual gas saturation and hydrate saturation. Residual gas entrapment is controlled by the aqueous-phase confinement of gas within dead-end pores, and residual gas accumulation is solely governed by the deterioration of pore connectivity and the development of dead-end pores. Equivalent volume growth rates are demonstrated by pore-filling and grain-coating hydrates. Both hydrate morphologies induce throat narrowing and pore network fragmentation, which contributes to the linear proliferation of dead-end pores at a steady generation rate.

Notably, after normalization, existing experimental data of residual gas in hydrate bearing sediments show high consistency with the proposed model. All evolutionary patterns conform to the linear model, with ε concentrating in the range of 4-6. In hydrate-bearing porous media, cross-study consistency in residual water and gas trends arises from universal physical mechanisms of capillary trapping and pore-structure modification. While these mechanisms ensure comparable normalized evolution patterns across independent investigations, limitations remain. First, compiled datasets vary in sediment lithology, grain-size composition, initial porosity, and hydrate-synthesis protocols, producing moderate dispersion in model coefficients. Furthermore, several datasets cover only partial hydrate-saturation ranges and fail to capture full-range evolutionary features. These discrepancies reflect geological heterogeneity among hydrate reservoirs and highlight the necessity of site-specific coefficient calibration prior to field-reservoir application of the model.

4. Conclusions

This study systematically investigates residual fluid saturation evolution in clayey silt hydrate bearing sediments, intriducing an experimental framework that distinguishes hydrate pore habits under gas-rich and water-rich conditions. The main conclusions are drawn as follows:

1) Hydrate saturation dominates residual saturation evolution. Residual-water saturation exhibits a two stage power-law growth with a transition at $S_h \approx 0.20$, whereas residual gas saturation increases linearly with hydrate saturation. For equivalent increments in hydrate saturation, residual-gas saturation rises 1.6-1.8 fold in water-rich relative to gas-rich environments, driven by the coupled effects of pore occupation, elevated capillary pressure, and expanded dead-end pores at higher S_h.
2) Initial porosity negatively governs residual saturation behavior. As initial porosity increases from 0.10 to 0.50, both residual water and residual gas saturation decrease monotonically, and such porosity-dependent disparities are markedly amplified at high hydrate saturation levels.
3) Hydrate pore habit constitutes the intrinsic origin of environment-driven residual saturation discrepancies. Residual water saturation differences between the two environments span a range of 0.06-0.22, while residual gas saturation differences range between 0.02-0.12. Relative to grain-coating and cementing hydrates in gas rich systems, pore-filling and load-bearing hydrates within water rich systems induce more pronounced pore structure modification and stronger fluid retention effects.
4) A quantitative evolution model for residual saturation is established, and its applicability is validated. Residual water saturation evolution follows a power-law relationship, which accurately characterizes the aforementioned two-stage growth pattern. Residual gas saturation evolution obeys a linear relationship and exhibits low sensitivity to hydrate pore habits.

This model is established for clayey silt lithology with constrained mineral compositions. Field reservoir applications require site-specific calibration using local core samples via a standardized workflow consisting of field multiphase displacement testing, model coefficient regression, and parameter substitution. Future studies are recommended to integrate *in-situ* pore imaging, natural core calibration, and multi-field coupling experiments to further strengthen the morphological basis and engineering applicability of the model.

Acknowledgments

This work was supported by the National Natural Science Foundation of China (No. 42606298), the Postdoctoral Fellowship Program of China Postdoctoral Science Foundation (No. GZB20260112).

References

Aghajanloo, M., Taghinejad, S., Voskov, D., et al. Influence of water saturation and water memory on CO_2 hydrate formation/dissociation in porous media under flowing condition. Chemical Engineering Journal, 2024, 492: 152455.

Agnissan, A., Guimpier, C., Terzariol, M., et al. Influence of clay-containing sediments on methane hydrate formation: Impacts on kinetic behavior and gas storage capacity. Journal of Geophysical Research: Solid Earth, 2023, 128(9): e2023JB027333.

Awag, M., Mackay, E., Ghanbari, S. Impact of CO_2 solubility on design of single well tracer tests to evaluate residual saturation during carbon capture and storage. Advances in Geo-Energy Research, 2024, 11(1): 6-19.

Cai, J., Berg, S. Recent advances in flow through porous media for energy exploitation. Energy & Fuels, 2025, 39(20): 9181-9184.

Cai, J., Xia, Y., Lu, C., et al. Creeping microstructure and fractal permeability model of natural gas hydrate reservoir. Marine and Petroleum Geology, 2020a, 115: 104282.

Cai, J., Xia, Y., Xu, S., et al. Advances in multiphase seepage characteristics of natural gas hydrate sediments. Chinese Journal of Theoretical and Applied Mechanics, 2020b, 52(1): 208-223. (in Chinese)

Cai, J., Yang, X., Yang, Z., et al. Microscopic flow and reactive transport in geological media: Recent advances and challenges. Capillarity, 2025, 17(3): 77-80.

Cao, S., Li, X., Jung, J., et al. Experimental techniques for studying interfacial dynamics and sediment response during CH_4-CO_2 hydrate replacement. Capillarity, 2025, 15(3): 53-57.

Cardona, A., Bhandari, A., Bhandari, A., et al. The viscoplastic behavior of natural hydrate-bearing sandy-silts under uniaxial strain compression (K0 Loading). Journal of Geophysical Research: Solid Earth, 2023, 128(7): e2023JB026976.

Chen, B., Chen, J., Wu, M., et al. Pressure and multiphase flow effects on CO_2 storage in hydrate-based cap: A comprehensive analysis. International Journal of Heat and Mass Transfer, 2026, 256(2): 127960.

Cheng, H., Lai, R., Liu, J., et al. Influence of roughness on spontaneous air-water imbibition in fractures: Insights from mathematical model analysis. Capillarity, 2025, 16(3): 87-94.

Dong, L., Liu, X., Gong, B., et al. Geomechanical properties of hydrate-bearing strata and their applications. Advances in Geo-Energy Research, 2025, 11(3): 161-167.

Fang, B., Zhang, Z., Zhang, Q., et al. Molecular insights into two-phase flow in clay nanopores during gas hydrate recovery: Wettability-induced multiple pathways of water lock formation. Advances in Geo-Energy Research, 2025, 17(1): 17-29.

Feng, Y., Qu, A, Han, Y., et al. Properties and model of pore-scale methane displacing water in hydrate-bearing sediments. Applied Energy, 2023, 349: 121694.

Gao, X., Lei, G., Zhao, Y., et al. A novel theoretical method for upscaling permeability in hydrate-bearing sediments. Water Resources Research, 2024, 60(10): e2024WR037729.

Geranutti, B., Pohl, M., Rathmaier, D., et al. Multiphysics measurements for detection of gas hydrate formation in undersaturated oil coreflooding experiments with seawa-

ter injection. Energies, 2024, 17(13): 3280.

Golsanami, N., Gyimah, E., Wu, G., et al. Laboratory synthesis and characterization of natural gas hydrates for sustainable gas production from hydrate-bearing sediments. Sustainability, 2026, 18(5): 2401.

Gong, B., Lei, G., Chen, L., et al. Mitigating risks in deep sea gas hydrate production: A new perspective on interpreting thermo-hydro-mechanical feedbacks. Advances in Geo-Energy Research, 2025, 17(3): 267-270.

Guo, D., Ou, W., Zhang, Y., et al. Hydrate formation and agglomeration in Pickering emulsions stabilized by hydrophilic and hydrophobic nano-$CaCO_3$ particles. Petroleum Science, 2025, 22(9): 3817-3829.

Jang, J., Narsilio, G., Santamarina, J. Hydraulic conductivity in spatially varying media–a pore-scale investigation. Geophysical journal international, 2011, 184(3): 1167-1179.

Jang, J., Sun, Z., Santamarina, J. Capillary pressure across a pore throat in the presence of surfactants. Water Resources Research, 2016, 52(12): 9586-9599.

Ji, Y., Kneafsey, T., Hou, J., et al. Relative permeability of gas and water flow in hydrate-bearing porous media: A micro-scale study by lattice Boltzmann simulation. Fuel, 2022, 321: 124013.

Jiang, Y., Zhang, R., Ye, R., et al. Mechanical properties of nodular natural gas hydrate-bearing sediment. Advances in Geo-Energy Research, 2024, 11(1): 41-53.

Joseph, J., Dangayach, S., Singh, D. et al. Investigation on excess gas method for synthesis of methane gas hydrates. Journal of Natural Gas Science and Engineering, 2017, 42: 203-215.

Kim, J., Lee, J., Ahn, T., et al. Validation of strongly coupled geomechanics and gas hydrate reservoir simulation with multiscale laboratory tests. International Journal of Rock Mechanics and Mining Sciences, 2022, 149: 104958.

Kou, X., Zhang, H., Chen, Z., et al. Dynamic mechanisms of gas hydrate evolution in hydrophobic sediments: Wall-climbing and secondary formation. Energy, 2026, 353: 141013.

Lei, J., Wang, Y., Guo, W. Fines migration characteristics of illite in clayey silt sediments induced by pore water under the depressurization of natural gas hydrate. Fuel, 2024, 365: 131236.

Lei, L., Seol, Y., Choi, J., et al. Pore habit of methane hydrate and its evolution in sediment matrix - Laboratory visualization with phase-contrast micro-CT. Marine and Petroleum Geology, 2019, 104: 451-467.

Li, M., Jian, Z., Hassanpouryouzband, A., et al. Understanding hysteresis and gas trapping in dissociating hydrate-bearing sediments using pore network modeling and three-dimensional imaging. Energy & Fuels, 2022a, 36(18): 10572-10582.

Li, S., Zhang, N., Hu, Z., et al. Visual experimental study on hydrate occurrence patterns and growth habits in porous media. Chemical Engineering Science, 2022b, 262: 117971.

Li, X., Xin, X., Xu, T., et al. Novel wellbore-reservoir coupling fluid flow model for natural gas hydrate production. Energy & Fuels, 2025a, 39(49): 23098-23112.

Li, Y., Xin, X., Liu, M., et al. An experimental study on gas-liquid phase fluid migration in hydrate-bearing sediments during hydrate dissociation. Engineering Geology, 2025b, 354: 108163.

Li, Y., Xin, X., Zhu, H., et al. Research progress and scientific challenges in permeability evolution of hydrate bearing sediments. Petroleum Science, 2025c, 22(12): 4895-4909.

Li, Y., Xu, T., Xin, X., et al. Multi-scale comprehensive study of the dynamic evolution of permeability during hydrate dissociation in clayey silt hydrate-bearing sediments. Advances in Geo-Energy Research, 2024a, 12(2): 127-140.

Li, Y., Xu, T., Xin, X., et al. Pore-scale study of the dynamic evolution of multi-phase seepage parameters during hydrate dissociation in clayey silt hydrate-bearing sediments. Journal of Hydrology, 2024b, 635: 131178.

Li, Y., Xu, T., Xin, X., et al. Effects of dipping and folded structure on gas production from hydrate bearing sediments. SPE Journal, 2024c, 29(2): 1129-1146.

Liu, M., Santamarina, J. Fracture sealing using precipitation reactions: Implications to long-term gas storage. Gas Science and Engineering, 2025, 153: 205962.

Liu, M., Seol, Y. A statistical and simulation-informed model for estimating permeability from pore size distribution in saturated geomaterials. Advances in Water Resources, 2025, 207: 105197.

Liu, W., Chen, Y., Shang, A., et al. Permeability anisotropy analysis of two-phase flow during hydrate dissociation process. Gas Science and Engineering, 2024, 126: 205342.

Liu, X., Li, Z., Liu, Y., et al. Surface sediment consolidation-creep characteristics in deep-sea mining areas: A quantitative microstructural perspective. Engineering Geology, 2025, 357: 108357.

Luo, Y., Sun, Y., Li, L., et al. Image-based pore-network modeling of two-phase flow in hydrate-bearing porous media. Energy, 2022, 252: 124044.

Lv, J., Zhao, J., Jiang, L., et al. A review of micro computed tomography studies on the gas hydrate pore habits and seepage properties in hydrate bearing sediments. Journal of Natural Gas Science and Engineering, 2020, 83: 103555.

Makogon, Y., Holditch, S., Makogon, T. Natural gas-hydrates–A potential energy source for the 21st Century. Journal of Petroleum Science and Engineering, 2007, 56(1-3): 14-31.

Meng, X., Liu, X., Zhang, H., et al. A physics-informed neural network framework for wave-induced dynamic response in a poroelastic seabed. Computers and Geotechnics, 2026, 198, 108250.

Rake, L., Pinkert, S. The effect of hydrate formation conditions on the mechanics of laboratory methane hydrate-bearing sediments. Journal of Geophysical Research: Solid Earth, 2024, 129(10): e2024JB029217.

Seol, Y., Kneafsey, T. Methane hydrate induced permeability modification for multiphase flow in unsaturated porous media. Journal of Geophysical Research: Solid Earth,

2011, 116: B08102.

Song, H., Zhao, J., Yin, Z., et al. Experimental study on metastable dissociation of sandy hydrate reservoirs. Chemical Engineering Science, 2024, 286: 119685.

Sun, H., Chen, J., Yang, X., et al. Characterizing methane hydrate phase transitions and multiphase flow behavior in porous media: Insights from low-field nuclear magnetic resonance measurements. International Journal of Heat and Mass Transfer, 2025a, 253: 127542.

Sun, H., Chen, J., Karunakaran, G., et al. System-level insights into flow-pressure-saturation coupling for safe and efficient methane hydrate production. Applied Energy, 2026, 411: 127623.

Sun, W., Kong, D., Li, Z., et al. Experimental investigation into gas migration mechanism in submarine sandy sediments at pore-scale. Advances in Geo-Energy Research. 2025b, 17(1): 30-42.

Takahisa, H., Konno, Y., Jin, Y., et al. Effect of heterogeneous hydrate distribution on permeability: Pore filling hydrate presents high permeability. Gas Science and Engineering, 2025, 142: 205682.

Terzariol, M., Park, J., Castro, G., et al. Methane hydrate-bearing sediments: Pore habit and implications. Marine and Petroleum Geology, 2020, 116: 104302.

Tiong, M., Peng, W., Liu, Q., et al. Natural gas hydrate exploitation: A comprehensive review of structural properties, technical progress and environmental challenges. Gas Science and Engineering, 2025, 144: 205769.

Waite, W., Santamarina, J., Cortes, D., et al. Physical properties of hydrate-bearing sediments. Review of Geophysics, 2009, 47: RG4003.

Wang, H., Li, Y., Huang, L., et al. A pore-scale study on microstructure and permeability evolution of hydrate-bearing sediment during dissociation by depressurization. Fuel, 2024a, 358(A): 130124.

Wang, S., Kong, D., Tan, J., et al. Mechanisms driving pathway-opening migration of gas in marine clayey sediments. Engineering Geology, 2025a, 348: 107965.

Wang, X., Yuan, Y., Du, Z., et al. Mineral effects on methane hydrate formation and distribution in sand sediments. Geoenergy Science and Engineering, 2024b, 243: 213379.

Wang, Y., Ma, R., Sun, Z., et al. A novel shifting framework to describe bimodal soil hydraulic properties. European Journal of Soil Science, 2025b, 76(6): e70243.

Wang, Y., Yang, J., Wang, P., et al. Impact of multiphasic pore-scale interactions on gas hydrate formation and dissociation characteristics and kinetics: A microfluidic study. Lab on A Chip, 2025c, 25(15): 3741-3765.

Wu, P., Chen, Y., Shang, A., et al. Anisotropy analysis of two-phase flow permeability in the multi-stage shear process of hydrate-bearing sediments. Energy, 2024, 293: 130697.

Wu, X., Qin, Y., Shi, H., et al. Erosion characteristics of hydrate-bearing sediments exposed to a cavitation jet. International Journal of Rock Mechanics and Mining Sciences, 2025, 191: 106118.

Xia, X., Elsworth, D., Xu, S., et al. Pore-scale gas-water two-phase flow and relative permeability characteristics of disassociated hydrate reservoir. Petroleum Science. 2025, 22(8): 3344-3356.

Xin, X., Liu, X., Xu, T., et al. Mechanical response of sandy and clayey-silty hydrate-bearing sediments in horizontal depressurization production. Energy & Fuels. 2026, 40(7): 3621-3636.

Xue, K., Yang, L., Zhao, J., et al. The study of flow characteristics during the decomposition process in hydrate-bearing porous media using magnetic resonance imaging. Energies, 2019, 12(9): 1736.

Yang, Z., Zhang, L., Jiang, Y., et al. Seepage-path-dependent CO_2 hydrate formation and storage capacity enhancement in NGH reservoirs. Fuel, 2026, 422: 139217.

You, Z., Wang, A., Jia, J., et al. Multistage triaxial shear behavior of methane hydrate-bearing sands: Insights from the discrete element method. Energy & Fuels, 2025, 39(39), 18831-18844.

Zhang, W., Luo, A., Wang, J., et al. A review on gas hydrate production feasibility for permafrost and marine hydrates. Journal Of Natural Gas Science and Engineering, 2022, 100: 104441.

Zhang, L., Song, W., Huang, F., et al. Hydrate stability assessment in marine environments: Implications for CO_2 sequestration site optimization. Journal of Environmental Chemical Engineering, 2026a, 14(2): 121641.

Zhang, Z., Guo, H., Hu, J., et al. Experimental insights into water flow path and relative permeability in porous media through visual microfluidic technology. Journal of Hydrology, 2026b, 668: 135021.

Zhang, J., Fu, H., Guo, M., et al. New insights into the deposition of natural gas hydrate on pipeline surfaces: A molecular dynamics simulation study. Petroleum Science, 2024a, 21(1), 694-704.

Zhang, Z., Liu, L., Lu, W., et al. Permeability of hydrate-bearing fine-grained sediments: Research status, challenges and perspectives. Earth-Science Reviews, 2024b, 244: 104517.

Zhao, Y., Liu, Z., Li, Y., et al. Subsidence characteristics of hydrate-bearing sediments during depressurization: Insights from experimental and discrete element method simulations. Energy & Fuels, 2024, 38(17): 16202-16217.